Cosmic Ray Spectrum from 250 TeV to 10 PeV using IceTop

(IceCube Collaboration)

In this analysis, we lower the energy threshold of IceTop from 2 PeV to 250 TeV, narrowing the gap between IceTop and direct measurements. To collect lower energy events, we implemented a new trigger that uses four pairs of infill stations for which the separation between stations is less than 50 m compared to 125 m for the main array. The new trigger collects data from the entire array for events with hits on at least one infill pair. Reconstruction of core position, direction, and energy of each shower is done with random forest regression. The IceTop all-particle cosmic ray energy spectrum is calculated assuming Sibyll 2.1 and QGSJetII-04 as the hadronic interaction models. Both measured energy spectra show a bend around the knee region. These spectra are compared with the energy spectrum from a previous IceTop analysis and other experiments.

I. INTRODUCTION

Cosmic rays are charged particles that reach Earth from space with energies as high as hundreds of EeV. The sources of high energy cosmic rays and their acceleration mechanism are not fully known, but they are reflected in the all-particle cosmic ray energy spectrum measured by ground-based air shower experiments. The differential energy spectrum is parameterized as a power law, $\frac{\mathrm{d}N}{\mathrm{d}E} \propto E^{-\gamma}$, where $\mathrm{d}N/\mathrm{d}E$ is the number of cosmic rays with energy between E and $E + dE$ and γ is the differential spectral index. Features in the spectrum correspond to changes in γ. Around $3{\times}10^{15}$ eV, γ increases from $\sim$2.7 to $\sim$3.0 and creates a knee-like structure, first mentioned in 1958 by Kulikov and Khristiansen [1]. Similarly, around 10^{18} eV, γ decreases from $\sim$3.0 to $\sim$2.7 and creates an ankle-like structure. This analysis covers the energy region around the knee.

The knee is believed to be the beginning of the end of cosmic rays from galactic sources. Since propagation and acceleration both depend on magnetic fields, the spectra of individual elements are expected to depend on magnetic rigidity [2]. The ankle is believed to be the energy region above which all cosmic rays are from extra-galactic sources [3].

The cosmic ray energy spectrum and its chemical composition are measured directly up to 100 TeV using detectors in satellites and balloons. They are indirectly measured by ground-based air shower experiments above 100 TeV as the rate of event drops sharply with the increase in energy. Therefore, a detector with a large exposure is required to detect enough cosmic rays in a reasonable time. There are several ground-based cosmic ray detectors sensitive to cosmic rays from a few TeV to hundreds of EeV. For example, ARGO-YBJ [4] detects cosmic rays in the energy range of a few TeV to a few PeV [5]. HAWC [6, 7] is a ground-based gamma ray and cosmic ray detector that measures cosmic rays from 10 TeV to 500 TeV [8]. Kascade [9], Tibet [10] and Tunka [11] are ground based detectors that measure the energy spectrum in the range of hundreds of TeV to hundreds of PeV [12–14]. Telescope array [15] and Pierre Auger Observatory [16] are ground-based detectors that detect ultra high energy cosmic rays with energy higher than 100 PeV [17, 18]. The combined energy spectra from all detectors provides an overview of the origin and the acceleration mechanism of cosmic rays.

The IceTop energy spectrum thus far covers an energy region from 2 PeV to 1 EeV [19, 20]. The goal of this analysis is to lower the energy threshold of IceTop to reduce the gap with direct measurements. A new trigger was introduced to collect events that trigger two stations in the more densely instrumented central area. In this way, the threshold of IceTop has been reduced to 250 TeV. Details of the new two-station trigger, which was turned on May 20, 2016, are discussed in section II. Data collected until April 2017 are used to calculate the energy spectrum. Two-station events are reconstructed using a random forest regression [21]. Monte Carlo simulations are used to train the random forest and develop a prediction model. The reconstruction method used in this analysis is discussed in detail in section IV.

This paper is divided into 5 sections. Section II describes the IceTop cosmic ray detector and the new two-station trigger implemented to collect low energy cosmic ray air showers. Section III discusses the data, both experimental and simulation, used for the low energy spectrum analysis. Section IV describes the reconstruction of air showers based on machine learning and reports the result of the all-particle cosmic ray energy spectrum. This section also describes details of the analysis, including quality cuts, unfolding method, pressure correction, and systematic uncertainties. The final section V summarizes the results. An appendix includes tables of systematic uncertainties and numerical values of the spectrum, as well as plots that illustrate the ability of the Monte Carlo to reproduce details of the detector response.

II. DETECTOR

IceTop is the surface component of the IceCube Neutrino Observatory [22, 23]. It detects extensive air showers produced by high energy cosmic rays. Data collected by IceTop are primarily used to measure the cosmic ray energy spectrum [19, 20, 24, 25], to study the mass composition of primary particles [20], and to calibrate In-Ice [26]. It has also been used to look for PeV gamma rays [27], solar ground level enhancements (GLEs) [28], and transient events, like solar flares [28] or gamma ray

bursts. There is an ongoing effort to use IceTop as a veto to reduce the background for astrophysical neutrinos [29].

IceTop is located at the South Pole at an altitude of 2835 m above the sea level. It consists of 162 tanks filled with clear ice distributed in 81 stations spread over an area of 1 km^2 as shown in Fig 1. Each station has two tanks separated by 10 m. Having two tanks in a station allows selection of a subset of events in which both tanks are hit. In this way it is possible to suppress the background of small showers hitting only one tank ($\sim$2 kHz [23]). Single tank hits in large showers are used to identify the muon component [30]. Stations are arranged in a triangular grid with typical spacing of 125 m. In addition, IceTop has a dense infill array where the distance between nearby stations is significantly smaller.

All tanks are made of 6 mm thick polyethylene by a rotational molding technique. A tank is a cylindrical container with an inner diameter of 1.82 m and a height of 1.1 m. All tanks were filled with water and frozen in using Freeze Control Units to form clear ice with a depth of 90 cm. Each tank is equipped with two Digital Optical Modules (DOMs) with different gains. The DOMs are partially immersed in water with the photo-multiplier tube (PMT) facing downward. Charged particles entering IceTop tanks produce Cherenkov light that is captured by PMTs.

The DOM is the fundamental detection unit for the IceCube Neutrino Observatory [22]. Each DOM is a glass pressure sphere of 33 cm diameter containing tools to detect, analyze, digitize, and communicate. The PMT [31] is the entry point of light into the data acquisition system (DAQ) [32]. A Field Programmable Gate Array (FPGA) controls data taking, triggering, digitization, and communication with the IceCube lab (ICL). An Analog Transient Waveform Digitizer (ATWD) is the electronics where signals are digitized. Each DOM also has a free-running 20 MHz oscillator used as a local timer. This oscillator is regularly calibrated with the master clock in the ICL. IceTop DOMs are fully integrated into the IceCube DAQ.

TABLE I. Four pairs of nearby infill stations and distance between each pair in meters. Each IceTop station has an assigned number from 1 to 81 as shown in Fig 1.

Stations	Distance [m]
46, 81	34.9
36, 80	48.9
36, 79	40.7
79, 26	41.6

The standard IceTop geometry is designed to detect cosmic rays in the energy range from PeV to EeV. The infill array is sensitive to cosmic rays with lower energy. The two-station trigger uses 4 pairs of closely spaced infill stations for which the separation between stations is less than 50 m (see Table I). The trigger condition is satisfied if any pair of stations is hit. If both tanks of a station are hit within 1 μs, then the "Hard Local Coincidence" (HLC) condition is fulfilled and if only one tank of a station is hit then "Soft Local Coincidence" (SLC) is said to be fulfilled. The two-station trigger is formed by counting the number of HLC hits in a window of 200 ns within a cylinder of 60 m centered around each tank. For an event to pass the trigger condition, it has to have 4 HLC hits within 60 m out of 12 high gain DOMs. Once the trigger condition is fulfilled, the readout window starts 10μs before and after the first and last of the 4 HLC hits. When the two-station trigger condition is satisfied, all hits in the entire IceTop array (both HLC and SLC) are collected. All triggered events automatically pass the filter condition and are sent to the North for analysis. The two-station event sample therefore includes events with ≥ 5 hit stations, as required for the standard IceTop event selection. Therefore the result of this low energy analysis can be compared to the higher energy IceTop results in a region of overlapping data.

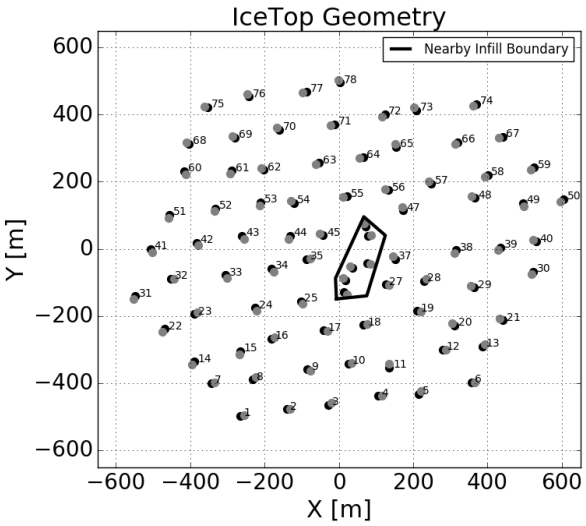

FIG. 1. IceTop geometry with positions of all tanks. The marked boundary in the center includes the six stations used to define the two-station trigger.

III. DATA

Experimental data were collected from May 2016 to April 2017 (IceCube year 2016) with a livetime of 330.43 days. A total of 7,420,233 two-station events is used after all quality cuts.

The energy of cosmic rays detected by a ground-based detector is not known directly. It has to be reconstructed from measured shower properties at the ground. To develop a method for shower reconstruction and to know its accuracy, simulations are used. Each simulated event depicts an air shower from a particle with a known type, position, direction, and energy. Simulations require a representation of the atmospheric profile and an event

generator for the hadronic interactions that make the shower. In this paper we use Sibyll2.1 [33] and QGSJetII-04 [34]. To simulate the atmospheric cascade, a standard simulation package called CORSIKA [35] is used. For simulation of propagation of particles through the tanks, Geant4 [36] is used.

CORSIKA simulations of proton, helium, oxygen, and iron primaries ranging from 10 TeV to 25 PeV in energy are used for this analysis. To increase statistics, the same CORSIKA shower is re-sampled multiple times by changing its core position. After re-sampling, there are approximately 100,000 showers for each 0.1 $\log_{10}(E/\mathrm{GeV})$ energy bin with zenith angle up to 65° (except for Helium and Oxygen between 10 TeV and 100 TeV for which the maximum angle is 40°). Events are generated uniformly in $\sin^2\theta$ bins, where θ is the zenith angle of primary particles. In the zenith region of interest ($\cos\theta \geq 0.9$), there are approximately 24,000 events in each 0.1 $\log_{10}(E/\mathrm{GeV})$. Sibyll 2.1 is used as the base hadronic interaction model for this analysis. CORSIKA showers with QGSJetII-04 as hadronic interaction model are also produced with 10% of the statistics compared to that of Sibyll 2.1. The QGSJetII-04 model is used to do a parallel study to compare its result with that of Sibyll2.1.

IV. ANALYSIS

This section describes the machine learning technique and features that are used to reconstruct two-station events. Quality cuts, iterative Bayesian unfolding, and systematic uncertainties are discussed and the cosmic-ray flux is presented.

A. Reconstruction

The reconstruction of air showers is done using random forest regression where simulations play a vital role. The quality of reconstruction depends on the quality of simulation. There must be a good agreement between simulations and experimental data. To check the quality of simulation, each feature of the experimental data used for the random forest regression is compared to simulation. As an example, Fig 2 shows the comparison of the distribution of x (left) and y (right) coordinate of tanks that are hit. Events used here are after all quality cuts, as described in subsection IV B. Both histograms are normalized. There is good agreement with all features of the experimental data. The ratio of simulation to data is also approximately 1 with some variation for position of tanks lying far from the shower core. Comparison between simulation and data for all other features show good agreement, as illustrated by the figures in the Appendix B. These plots show a good agreement between experimental data and simulations with Sibyll 2.1 as the hadronic interaction model. Therefore, simulations generated for this analysis can be used with good confidence to develop a model using random forest regression to reconstruct air showers.

Random forest regression is the algorithm used in this analysis for reconstruction of the core position, zenith angle, and energy of two-station events. A detailed description of random forest regression is found in [37]. A random forest is a 'forest' made up of many decision 'trees'. The formation of a decision tree involves recursively splitting data into two parts. The split is done based on a feature that minimizes the Residual Sum of Squares (RSS) at each node. To decide which feature minimizes the RSS, data are divided into two parts by various values of each feature used. The RSS are calculated on both parts and are added. Then all summed RSS for all values and all used features are compared. The final split of data at a node is done by a feature at a value that produces the minimum summed RSS. As an example, assume there are n1 and n2 events after splitting data by a feature at a value while predicting energy. Assume $\hat{E}_1$ is the mean true energy of n1 events and $\hat{E}_2$ is that for n2 events. The summed RSS is given by

$$RSS_{\mathrm{sum}} = \sum_{i=1}^{n1}(E_i - \hat{E}_1)^2 + \sum_{i=1}^{n2}(E_i - \hat{E}_2)^2 \qquad (1)$$

where E_i is true energy of event i that ends up in one of the two groups. Once the data is split into two parts, the process is repeated by further splitting the split data. Again a split is done based on a feature and its value that minimizes summed RSS.

Branching of data by splitting it multiple times leads to a tree-like structure. The end of a tree is called a leaf. The branching process continues until a stopping criterion is reached. There are two commonly used stopping criteria. The first is the maximum number of branches in a tree, which is commonly known as the depth of a tree. The second is the minimum number of events at a leaf of a tree. If one of these criteria is fulfilled then the splitting process is complete. Each leaf of a tree uses the mean of the true value from events that land in that leaf and assigns that mean value as its prediction.

A forest has many decision trees. Variation among trees comes from using randomly selected subsets of features and data. A decision tree is grown by considering randomly selected features at each split. The number of features used is usually equal to the square root of total number of features. Data are also randomly selected by a bootstrapping method. The number of bootstrapped datasets is equal to the number of trees in a forest. During training the algorithm randomly selects data used to grow a tree so that each decision tree is slightly different. Combining the predictions from each tree reduces the variance of the prediction [21]. Finally, the unknown quantity is predicted by knowing which leaf the event lands on in each tree and taking an average of their predicted values.

Various features of an air shower are used to predict (reconstruct) core position, zenith angle, and energy. The features used for reconstruction of air showers

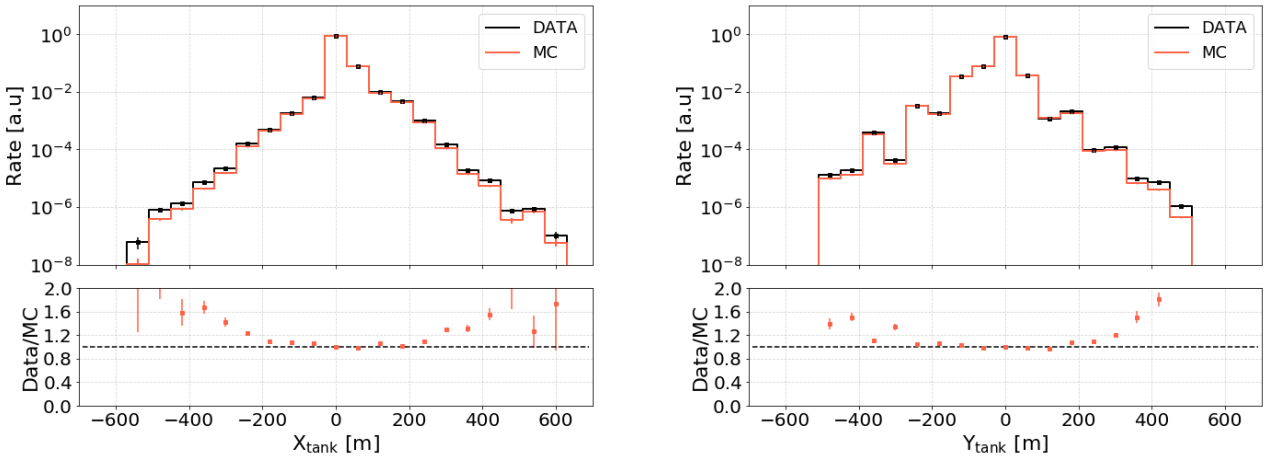

FIG. 2. Histograms of x (left) and y (right) coordinate of tanks hit in data compared with simulations. Even the small features in histogram of simulations are similar in the data.

TABLE II. List of all features that go into the random forest regression and their description. Refer to the text below for detailed descriptions of all features.

Features	**Description**
X_{tank}, Y_{tank}	List of X and Y coordinate of hit tanks that of each event.
X_{COG}, Y_{COG}	X and Y coordinate of shower core's center of gravity.
θ_{plane}	Zenith angle assuming a plane shower front.
ϕ_{plane}	Azimuth angle assuming a plane shower front.
$\cos\theta_{plane}$	Cosine of θ_{plane}.
$\cos\theta_{reco}$	Cosine of reconstructed zenith angle.
T_0	Time at the shower core when shower core assuming plane shower front hits the ground.
ZSC_{avg}	Average distance of hit tanks from a plane shower front. Ideally a ZSC_{avg} of a vertical shower is 0 and that of horizontal shower is maximum.
R_{tank}	List of distance of hit tanks from the reconstructed shower core of each event. Each distances is divided by 60 m.
logNsta	log10 of number of stations hit.
$\log Q_{total}$	log10 of total charge deposited in all stations that are hit.
Q_{sum2}	Sum of first two highest charge deposited in tanks that are hit.
Q_{tank}	List of charge deposited on tanks that are hit of each event. This is a list of all 'Q_i' in equation 2.
T_{tank}	List of time of hit on tanks of each event. This is a list of all 't_i' in equation 3 with respect to the first hit time.

in this analysis are discussed below and summarized in Table II. Not all input features are equally important. Some features are good at predicting an unknown quantity while others do not help. A feature that is used more times to split data has a higher feature importance. Random forest regression commonly uses a mean decrease in impurity (MDI) method to calculate a feature's importance. It is based on how effective the feature is to reduce variance while forming decision trees of a random forest. MDI and other techniques used to calculate feature importance are discussed in [37, 38]. Permutation importance method is implemented to calculate feature importance while predicting energy in this analysis. In this method, the importance of a feature is calculated by randomly permuting its value and calculating R^2 score before and after permuting. The difference of R^2 score before and after permutation is the importance of that feature. All features and their importance to predict core position, zenith angle, and energy are shown in Fig 3 and described below.

We arrange the position of tanks based on their corresponding charges, largest to smallest. These lists are denoted by X_{tank} and Y_{tank} representing the x and y coordinate, respectively. They have the highest feature importance for determining the core position. The shower core is the position where the shower axis hits the ground.

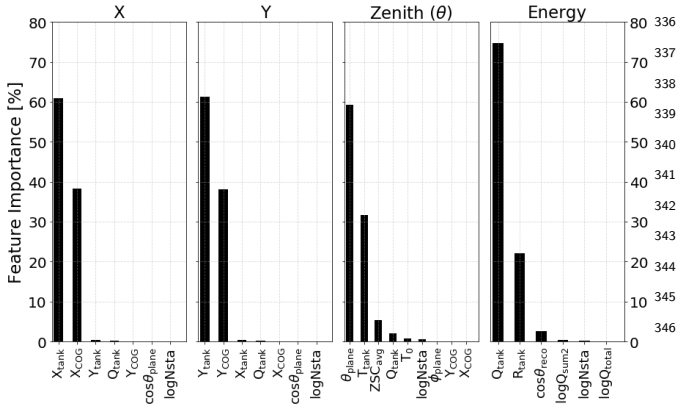

FIG. 3. Feature importance to predict x and y coordinate of core position, zenith angle, and energy. Lists of coordinates of hit tanks ($X_{\rm tank}$, $Y_{\rm tank}$) have the highest feature importance for core position. The zenith angle assuming a plane shower front ($\theta_{\rm plane}$) and time of hits (T_{tank}) have the highest feature importance for zenith angle. The list of charge on hit tanks ($Q_{\rm tank}$) and their distance from the shower core ($R_{\rm tank}$) have the highest feature importance for energy.

A first guess of shower core position can be calculated as the weighted sum of positions of tanks that have been hit. The weight used is the square root of the charge on an individual tank. The x-coordinate of the shower center of gravity (COG) is given by

$$X_{\rm COG} = \frac{\sum_i \sqrt{Q_i} x_i}{\sum_i \sqrt{Q_i}} \qquad (2)$$

where i runs over tanks that have been hit, Q_i is the charge on tank i, and x_i is the x-coordinate of tank i. Similarly, $Y_{\rm COG}$ is calculated using the y-coordinates of hit tanks. As shown in Fig 3, COG has the second highest feature importance for predicting the shower's core position after the coordinates of hit tanks ($X_{\rm tank}$, $Y_{\rm tank}$).

A first guess for the direction of a shower can be calculated by assuming a plane shower front traveling perpendicular to the shower axis. This direction is a good approximation for events with a small number of hit tanks. The quantities of interest are zenith angle (θ) and azimuth angle (ϕ) of the air shower. The initial reconstruction is done by minimizing chi-square given by

$$\chi^2(n_x, n_y, t_0) = \sum_i \frac{(t_i - T_0 + \frac{n_x x_i + n_y y_i}{c})^2}{\sigma_i^2} \qquad (3)$$

where t_i is the measured signal time at each tank, T_0 is the time the core hits the ground, $n_x = \sin\theta\cos\phi$, and $n_y = \sin\theta\sin\phi$. The sum runs over all hit tanks. The time uncertainty σ_i is equal to 5 ns for all tanks [23]. The plane fit direction is $\theta = \cos^{-1}(-\sqrt{1-n_x^2-n_y^2})$ and $\phi = \tan^{-1}(\frac{n_y}{n_x})$. As shown in Fig 3, $\theta_{\rm plane}$ has the highest feature importance for predicting the zenith angle of a shower, and the time of hits ($T_{\rm tank}$) is second. $T_{\rm tank}$ denotes the list of times at which tanks have been hit for each event. The time of the first hit of an event is subtracted from all hits such that the time used is with respect to the first hit. The time information of an event is arranged in ascending order. If an event has fewer than 35 hits (see below), then the remaining slots are filled with the last relative time. $ZSC_{\rm avg}$ is the average distance of hit tanks from the plane shower front when the core hits the ground. $ZSC_{\rm avg}$ is higher for inclined showers and approximately zero for vertical showers. It is given by

$$ZSC_{\rm avg} = \frac{\sum_{i=1}^{n} |z_i|}{n} \qquad (4)$$

where i runs over n hit tanks and z is the position of a tank in the shower coordinate system. As shown in Fig. 3, $ZSC_{\rm avg}$ also has some importance for predicting shower's zenith angle.

For reconstruction of energy, $Q_{\rm tank}$ has the highest feature importance. It is defined by forming a list of charges on all n tanks that have been hit and sorting them in descending order. The minimum value that n can have is 4 and it can increase up to 162. For the energy region of interest, information from the first 35 hits is enough to reconstruct shower core position, direction, and energy with almost 100% feature importance. The random forest regression becomes computationally expensive as the number of features increases. Therefore, the number of items per event in each list is truncated to 35 from 162. If the number of tanks (n) that have been hit is less than 35, then the remaining 35-n slots of the list are filled with 0 for $Q_{\rm tank}$, $X_{\rm tank}$, and $Y_{\rm tank}$. Second most important feature is $R_{\rm tank}$, defined as an array of the distance from the shower core of each tank that has been hit. Each distances is divided by a reference distance of 60 m. The total number of hit stations ($N_{\rm sta}$) in each event, the sum of charges ($Q_{\rm total}$) from all hit tanks, and the sum of the two highest charges ($Q_{\rm sum2}$) of an event are also used to reconstruct energy, but have relatively small importance. Charge is calibrated in units of vertical equivalent muons (VEM) and is defined as a total charged deposited by a single vertical muon passing through an IceTop tank. Refer to [23] for a detail description of VEM for the IceTop detector.

Random forest regression trains on many decision trees separately, so the training can be done in parallel. Spark [39] is a fast cluster computing technology designed to run jobs in parallel. Random forest regression from Spark is used separately to reconstruct core position and zenith angle. Similarly the reconstruction of energy is done using random forest regression from Scikit-Learn [40].

The quality of reconstruction is judged based on how good the resolution is. Fig 4 shows core resolution, zenith resolution, and energy resolution. The core resolution is about 16 m, the zenith resolution is about 4°, and the energy resolution is about 0.26 for the lowest energy bin ($\log_{10}[E/{\rm GeV}]$ 5.4 to 5.6). All three resolutions improve

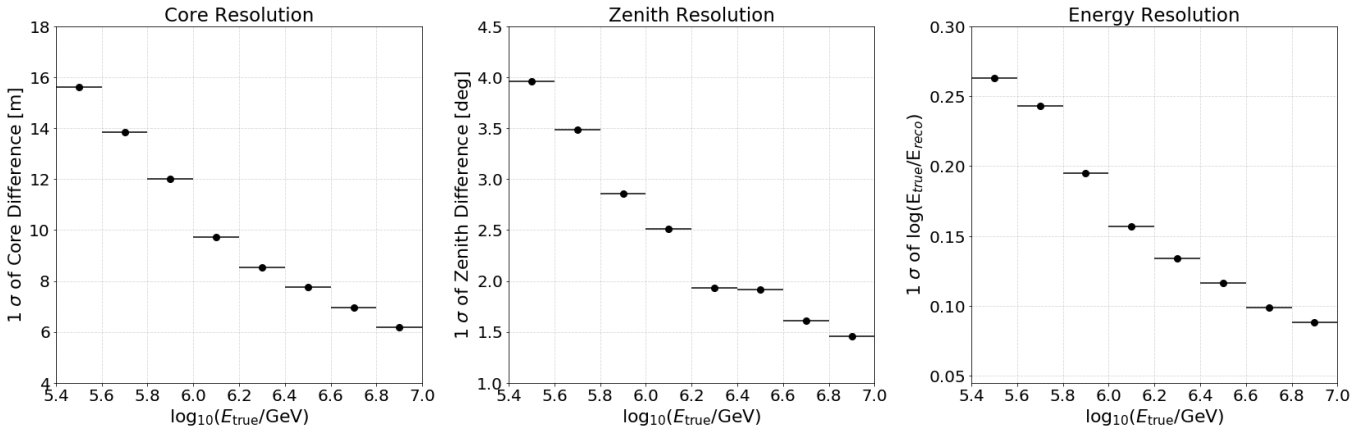

FIG. 4. Left: Core resolution in meters; Middle: zenith resolution in degrees; Right: energy resolution in unit-less quantity. See Table III for resolution values.

as energy increases. Resolutions for each energy bin are given in Table III of Appendix A.

B. Quality Cuts

Only well-reconstructed events are used to obtain the energy spectrum. Quality cuts are used to remove events with possible bad reconstruction to reduce error and to improve accuracy. The passing rate of events for a cut is the percentage of events surviving that cut and all previous cuts. The following cuts are applied to the simulated and the experimental data to select events:

- Events must pass the two-station trigger and filter. Passing rate for this cut is 100% by definition.
- Events must have the tank with the highest charge inside the nearby infill boundary. This cut is designed to select events with shower cores inside or near the infill boundary. Passing rate for this cut is 89.5%.
- Events must have cosine of zenith angle (θ) greater than or equal to 0.9. These events have higher triggering efficiency and are better reconstructed. Passing rate for this cut is 48.1%.
- Events with most of the energy deposited only in few tanks are removed, as they are known to be poorly reconstructed. This cut requires the largest charge to be less than or equal to 75% of the total charge and the sum of the two largest charges less than or equal to 90% of the total charge. Passing rate for this cut is 36.836%.
- The simulation used for this low energy analysis extends to $\log_{10}(E/\mathrm{GeV})$=7.4. From the simulation we have determined that events with a true energies above that can be removed by excluding events with more than 42 stations hit and excluding events with a total charge greater than $10^{3.8}$ VEM. We also excluded events with a total charge less than 0.63 VEM to remove events due to background noise. Passing rate for this cut is 36.835%.

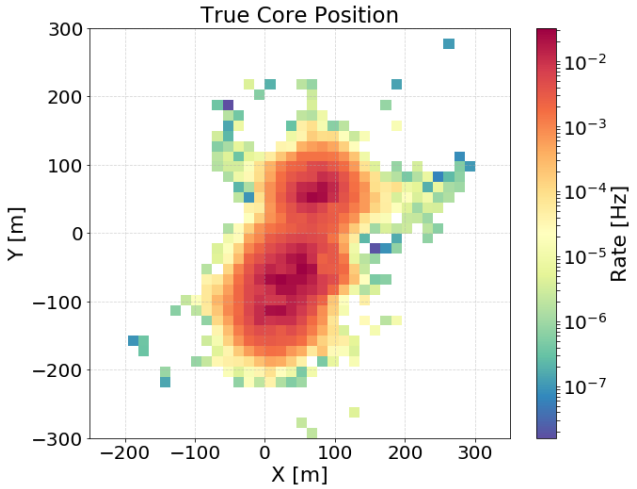

FIG. 5. Histogram of true core position of showers after all quality cuts.

The histogram of true core position of events that pass all quality cuts is shown in Fig 5. Most events lie within a radius of 300 m after all quality cuts.

C. Bayesian Unfolding

One of the challenges that a ground-based detector faces is to know the true energy distribution (C, Cause) from the reconstructed energy distribution (E, Effect). Iterative Bayesian unfolding [41, 42] is used to take energy bin migration into account and to derive the true from the reconstructed energy distribution. It is implemented via a software package called pyUnfolding [43].

This package also calculates and propagates error in each iteration.

To unfold the energy spectrum, the response of the detector to an air shower is required. The response is determined from simulations. This information is stored in a response matrix and is the probability of measuring a reconstructed energy given the true primary energy. The response matrix used in this analysis is shown in Fig. 6. Inverting the response matrix to get a probability of measuring true energy given reconstructed energy would lead to unnatural fluctuations. Therefore, Bayes theorem is used iteratively to get the true distribution from athe observed distribution.

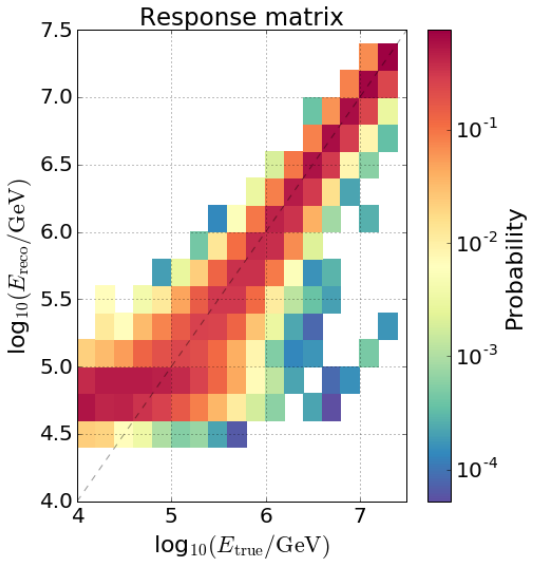

FIG. 6. Response Matrix calculated from simulation. An element of a response matrix is a fraction of events in true energy bin distributed over the reconstructed energy bin. In Bayes theorem of Eq. 5, $P(E|C)$ represents a response matrix.

The Bayes theorem is given by

$$P(C_\mu|E_i) = \frac{P(E_i|C_\mu)P(C_\mu)}{\sum_\nu^{n_C} P(E_i|C_\nu)P(C_\nu)} \tag{5}$$

where $P(C|E)$ is the unfolding matrix, $P(E|C)$ is the response matrix, n_C is the number of cause bins, and $P(C)$ is the prior knowledge of the cause distribution. $P(C)$ is the only quantity that changes in the right-hand side of Eq. 5 during each iteration. The choice of initial prior, $P(C)$, is optional and can be any reasonable distribution, like a uniform distribution or $n(E)/\sum_i^{n_E} n(E_i)$. The conventional choice to minimize bias is Jeffreys' Prior [44], given by

$$P_{\rm Jeffreys}(C_\mu) = \frac{1}{\log_{10}(C_{\rm max}/C_{\rm min})C_\mu} \tag{6}$$

Each iteration produces a new unfolding matrix $P(C|E)$. $P(C_\mu|E_i)$ represents the probability that an effect E_i is a result of cause C_μ. If the distribution of effect $n(E)$ is known then the updated knowledge of the cause distribution is given by

$$\phi(C_\mu) = \frac{1}{\epsilon_\mu}\sum_i^{n_E} P(C_\mu|E_i)n(E_i) \tag{7}$$

where $\epsilon_\mu = \sum_j^{n_E} P(E_j|C_\mu)$ and $0 \leq \epsilon_\mu \leq 1$. It must be noted that ϵ_μ in this analysis is equal to 1. $\phi(C_\mu)$ in Eq. 7 is used to calculate an updated prior. The updated prior is given by

$$P(C_\mu) = \frac{\phi(C_\mu)}{\sum_\nu \phi(C_\nu)}$$

which is then used as a new prior in equation 5 for the next iteration. The unfolding proceeds until a desired stopping criterion is satisfied. The commonly used stopping criteria are χ^2 and Kolmogorov-Smirnov of subsequent energy distribution before and after unfolding. In this analysis, Kolmogorov-Smirnov less than 10^{-3} is used as the stopping criterion. It is reached in the twelfth iteration.

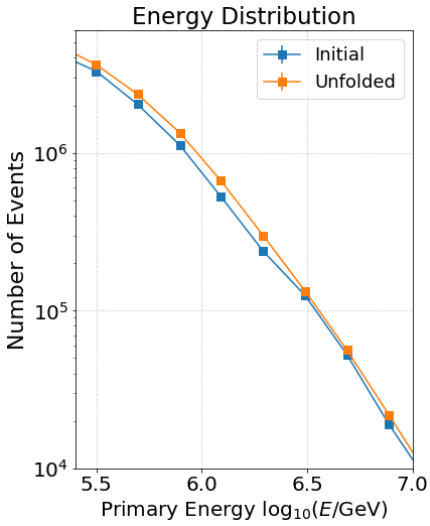

FIG. 7. Energy distribution before and after iterative Bayesian unfolding. Blue is the reconstructed energy distribution and orange is the final unfolded energy distribution.

Each iteration generates a new cause distribution $\phi(C)$. Using this to calculate the next prior can propagate error, if any, in each iteration which might cause erratic fluctuations on the final distribution. To regularize the process and to avoid passing an unphysical prior in each iteration, the logarithm of the cause distribution ($\phi(C)$) is fitted with a polynomial except for the final distribution. The final unfolded energy distribution is used to calculate the cosmic ray flux. The reconstructed energy distribution $n(E)$ in Eq. 7 and the final unfolded energy distribution are shown in Fig 7.

D. Pressure Correction

The rate of two-station events fluctuates with changes in atmospheric pressure. If pressure increases, the rate decreases and vice-versa. If the average pressure during which data were taken is not equal to the pressure of the atmospheric profile used in the simulation, then the final flux must be corrected to account for the difference in the atmospheric pressure between data and simulation.

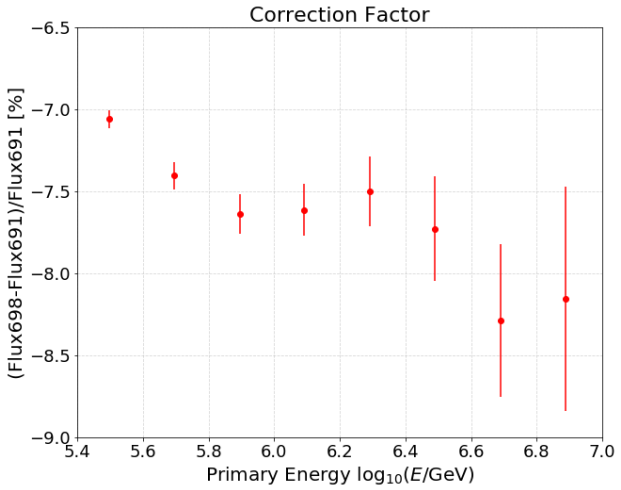

FIG. 8. Percentage deviation of cosmic rays flux when atmospheric pressure is $\sim$698 g/cm^2 from the flux when pressure is $\sim$691 g/cm^2. This deviation is used as the correction factor to correct the final flux. The error on the correction factor is used as the systematic uncertainty due to Pressure difference between average pressure of 2016 South Pole atmosphere and pressure due to atmosphere profile used in simulation.

The average pressure at the South Pole during data-taking was 678.27 hPa (data obtained from Antarctic Meteorological Research Center). This converts to $1.019 \times 678.27 = 691.16\, g/cm^2$.

In CORSIKA, the density variation of the atmosphere with altitude is modeled in 5 layers. At the altitude h (cm) from sea level, the overburden $T(h)$ of the atmosphere is given by the form

$$T(h) = a + b\exp(-\frac{h}{c}) \quad (8)$$

For the energy region of interest in this analysis, the average April atmosphere was used for which the parameters are $a = -69.7259$, $b = 1111.7$, and $c = 766099$. With these parameters for IceTop at an altitude of 2835 m above sea level, $T(h)$ is $698.12\, g/cm^2$. This is $\sim$1% larger than the average pressure for the period of data-taking (698.12/691.1).

During the period 08 January 2017 to 28 April 2017 the average pressure was 698.12 g/cm^2, the same as that used in the simulation. The flux from this subset of data is calculated and compared with the flux for the entire data-taking period. The flux decreases with an increase in pressure and this decrease must be corrected. The correction factor is shown in Fig. 8 and tabulated in Table IV, Appendix A. Errors on the correction factors due to pressure difference are used as the systematic uncertainty on flux due to atmospheric pressure. There are at least two factors that contribute to the correction. At higher pressure, the size at ground for a given energy is smaller. In addition, the shower is more spread out, decreasing the trigger probability. The correction shifts the flux down.

E. Systematic Uncertainties

Systematic uncertainties are calculated by keeping all conditions constant except the feature under investigation. The systematic uncertainties due to the hadronic interaction models are considered separately. The major systematic uncertainties, excluding those due to hadronic interaction models, are those due to the composition, the unfolding method, the effective area, and the atmosphere. Individual and 'total systematic uncertainty' are shown in Fig 9.

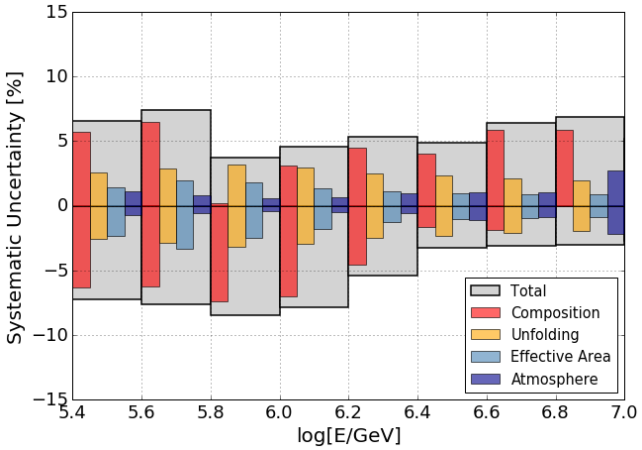

FIG. 9. The plot shows the individual systematic uncertainties for each energy bin. The total systematic uncertainty is the sum of individual uncertainties added in quadrature.

To estimate the uncertainty due to composition, the Gaisser H4a model [45] is used as a base composition model and GST [46], GSF [47], and a version of Polygonato modified to include an additional higher energy Galactic population B are used as alternate models. Since all these models are viable options for composition, the flux for each model is calculated using the same response matrix, and the percentage deviation of the flux from the model for each energy bin is measured. Additionally, the fractional difference between fluxes calculated for two extreme zenith bins is used to calculate composition systematics as done for the 3-year energy spectrum analysis. The maximum spread of all deviations is used as the uncertainty due to composition.

The pyUnfolding package calculates the systematic uncertainty due to unfolding at the end of each iteration. The uncertainty arises from the limited statistics of the simulated data set. Evolution of systematic uncertainty after each iteration is saved. In this study, we need 12 iterations before reaching the termination criterion. The systematic uncertainty for the twelfth iteration is used as the systematic uncertainty from the unfolding procedure.

The effective area is fitted with an energy-dependent function given by

$$A_{\rm eff}(E) = \frac{p_0}{1 + {\rm e}^{-p_1(\log E - p_2)}} \tag{9}$$

The parameters of the fit contain errors and the errors have to be accounted for while calculating flux. A band around the effective area fit is shown in Fig. 10 after accounting for all errors on the parameters. Taking the upper and lower boundary of the band, the flux is calculated and the difference in the flux is used as the systematic uncertainty due to effective area.

The correction factor to account for the atmospheric pressure difference between data and simulation is shown in Fig 8. The uncertainty on the correction factor is used as the systematic uncertainty due to pressure. Also, the difference in flux due to different temperatures for constant pressure is used as the systematic uncertainty due to temperature and is less than 2%. These two uncertainties are added and the summation is used as the systematic uncertainty due to the atmosphere.

Different snow heights for data and simulation would affect the low energy spectrum analysis. Experimental data used in this analysis is from May 2016 to April 2017 and the snow height used for simulations is from October 2016 in the middle of the data sample. Thus the average height of snow for the experimental data is assumed to be comparable to that used in the simulation. VEM calibration occurs monthly. Systematic uncertainties arising from VEM calibartion and duration have been studied and are small.

The statistical uncertainty is small due to the large volume of data. The systematic uncertainty from the composition assumption is the largest, while the systematic uncertainties from the unfolding method, effective area, and atmosphere are relatively small. The 'total systematic uncertainty' is calculated by adding individual contributions in quadrature and is larger than the statistical uncertainty. The total systematic uncertainty for each energy bin is tabulated in Table V of Appendix A.

F. Flux

The cosmic-ray flux, or energy spectrum, is the distribution of cosmic rays by energy. Once the core position, direction, and energy of air showers are reconstructed, and the effective area is known, the flux is calculated. The binned flux is given by

$$J(E) = \frac{\Delta N(E)}{\Delta \ln E \pi (\cos^2\theta_1 - \cos^2\theta_2) A_{\rm eff} T} \tag{10}$$

where $\Delta N(E)$ is the unfolded number of events with energy per logarithmic bin of energy in time T, $[\theta_1, \theta_2]$ is the observed zenith range, and $A_{\rm eff}$ is the effective area. The effective area for IceTop events with $\cos\theta \geq 0.9$ is shown in Fig 10 and is used to calculate the flux. The livetime (T) is 28548809.85 s (330.43 days), $\Delta \log_{10} E$ is 0.2, and $\cos\theta_1$ and $\cos\theta_2$ used are 1.0 and 0.9 respectively.

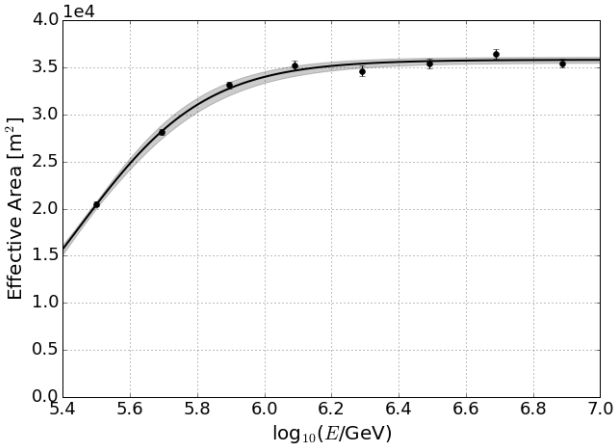

FIG. 10. Effective area calculated using MC generated with H4a composition model and Sybill 2.1 hadronic interaction model. A sigmoid function is used to fit the effective area.

The all-particle cosmic ray flux is calculated using Eq. 10 in the energy range 250 TeV to 10 PeV. The calculated flux is corrected for pressure difference using the correction factors shown in Table IV of Appendix A. The final flux is then compared with the higher energy measurement of IceCube [20] in the left plot of Fig 11. The spectrum is plotted per logarithmic bin of energy in units of $\rm m^{-2}s^{-1}sr^{-1}$.

The effect of the hadronic interaction model is not included in the 'total systematic uncertainty'. Instead, the same analysis steps were repeated using simulation with QGSJetII-04 as the hadronic interaction model. The statistics of the simulation for the analysis with QGSJetII-04 is only 10% of that for Sibyll 2.1 but is sufficient for the comparison between the two models. The right plot of Fig 11 shows the comparison between fluxes assuming Sibyll2.1 and QGSJetII-04 as hadronic interaction models and their ratio. The flux assuming QGSJetII-04 is comparable with the flux assuming Sibyll2.1 at the lower energy region and is around 20% lower above the knee.

Many ground-based cosmic ray detectors measured the cosmic ray flux around this energy region. Several measurements with their statistical uncertainties are compared with the result of this analysis in Fig 12. The range of fluxes reflects systematic uncertainties in the

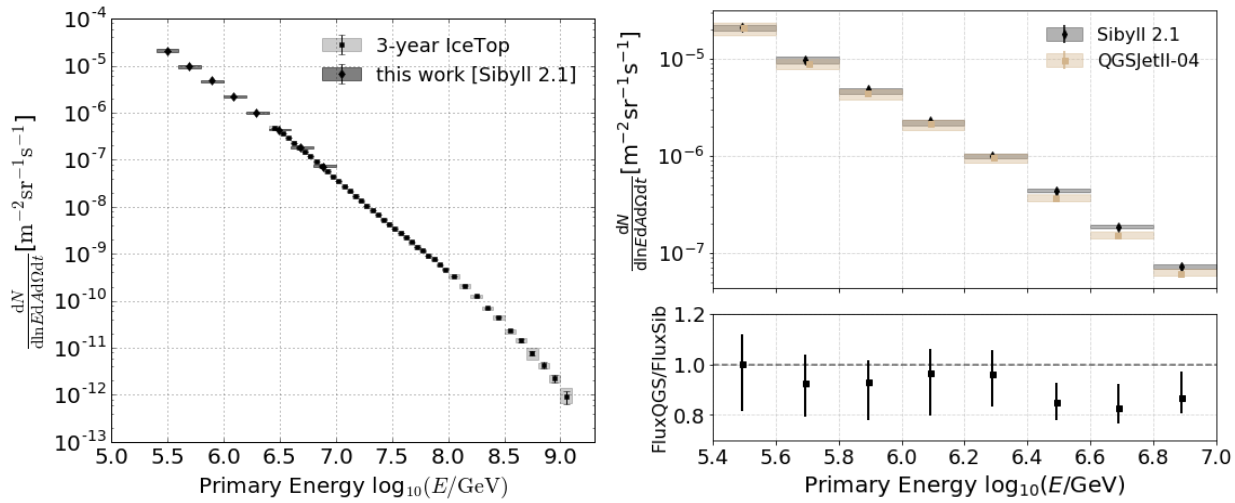

FIG. 11. Left: The all-particle cosmic ray energy spectrum using IceTop 2016 data. The analysis is done using simulations with Sibyll 2.1 as the hadronic interaction model. Right: The all-particle cosmic ray energy spectra using simulations with Sibyll2.1 and QGSJetII-04 as hadronic interaction models. The same analysis as with Sibyll 2.1 was repeated with QGSJetII-04. The shaded region in both plots indicates the systematic uncertainties.

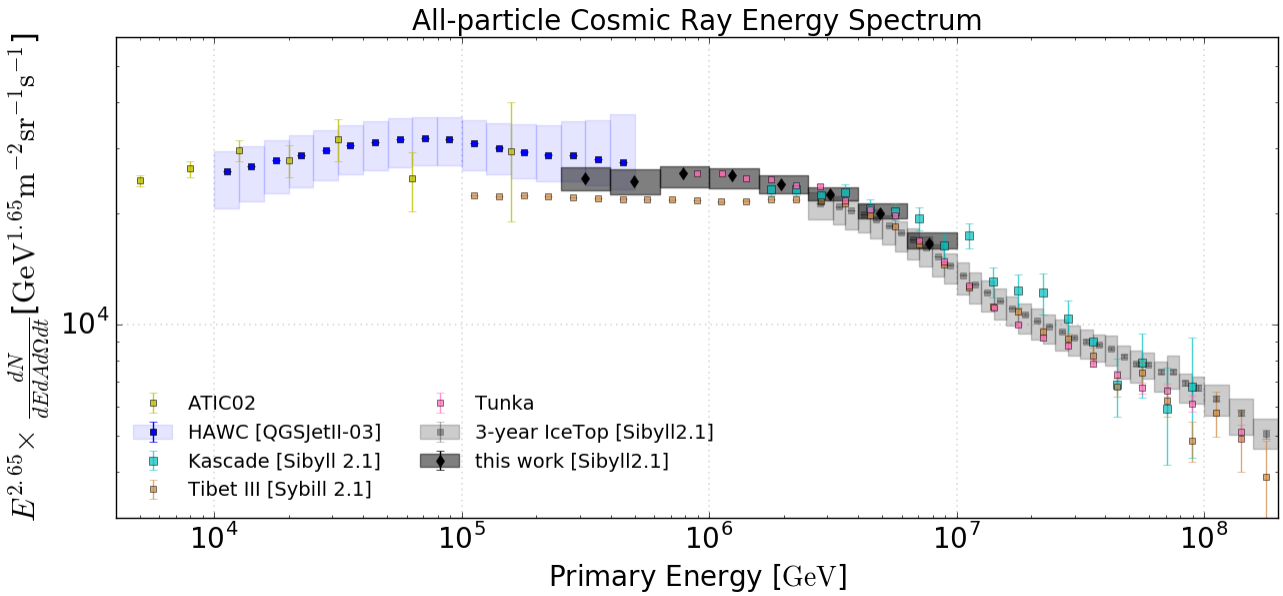

FIG. 12. Cosmic Ray Flux using IceTop 2016 data scaled by $E^{1.65}$ and compared with flux from other experiments. This analysis and HAWC's energy spectrum analysis use different hadronic interaction models. The shaded region indicates the systematic uncertainties.

measurements. Since the cosmic ray flux follows a steep power law, a slight difference in energy scale can cause a large difference in the flux. The IceTop low energy spectrum extension overlaps with the results from HAWC [8] in the lower energy region and with Kascade [48] and Tunka [49] measurements at higher energy region, and is higher than the result from Tibet III [50]. The low energy spectrum is also compared with a direct measurement from ATIC-02 [51].The hadronic interaction model is different for HAWC and for this analysis, which can contribute to the difference between the results shown for these experiments.

V. RESULT AND DISCUSSION

The principal result of this paper is to lower the energy threshold for the measurement of the all-particle spectrum with IceTop. Most effort went into the deployment of a new trigger to select low energy events and

into the development of a new reconstruction method for these hard to reconstruct events. This analysis measured the all-particle cosmic ray energy spectrum from 250 TeV to 10 PeV, lowering the energy threshold of IceTop from ∼2 PeV to 250 TeV.

Table VI in Appendix A tabulates the result of the IceTop low energy spectrum analysis. The first column is the energy bin in $\log_{10}[E/\mathrm{GeV}]$. The second column is the number of events in reconstructed energy bins before unfolding. The total number of events in these energy bins is 7,420,233. The third column is the rate of events before unfolding calculated by dividing the second column with livetime. The fourth column is the unfolded rate. The fifth column is the all-particle cosmic ray flux calculated from the unfolded rate. The remaining columns are the statistical uncertainty, the lower systematic uncertainty, and the upper systematic uncertainty in the flux respectively. Corresponding results assuming QGSJetII-04 as the hadronic interaction model are shown in Table VII of Appendix A.

The final energy spectrum from this analysis is shown in figures 11 and 12. The figures show that the flux is somewhat higher than the 3-year IceTop spectrum in the overlap region. These two fluxes are fitted with splines to calculate their percentage differences at each energy bin of the 3-year analysis up to 10 PeV. The energy spectrum from this analysis is within 7.1% of the 3-year IceTop spectrum. The total systematic uncertainty by adding individual uncertainties in quadrature for the 3-year spectrum is 9.6% at 3 PeV and 10.8% at 30 PeV [19]. Even though the flux is higher, it is within the systematic uncertainty of 3-year IceTop energy spectrum analysis. Both analyses use data collected by IceTop, so they share systematic uncertainties related to the detector. However, there are differences in this analysis, such as the treatment of the pressure correction and the unfolding that contribute to the systematics. Other important differences are in data taking (trigger/filter) and in the use of machine learning for reconstruction.

The right plot of Fig 11 shows the difference in fluxes assuming two different hadronic interaction models, i.e. Sibyll2.1 and QGSJetII-04. The flux assuming QGSJetII-04 is approximately 20% lower than the flux assuming Sibyll2.1 above the knee.

The low energy extension of the IceTop all-particle cosmic ray energy spectrum includes the entire knee region of the spectrum. It extends the 3-year IceTop spectrum [20] into the region below 2 PeV to give a full view of the spectral change associated with the knee. Additionally, the energy spectrum overlaps with HAWC's result [8] within the systematic errors around 300 TeV. The energy spectrum measured in this analysis fills the gap between the 3-year IceTop spectrum and the HAWC measurements and thus connects with direct measurements.

ACKNOWLEDGMENTS

The IceCube collaboration acknowledges the significant contribution to this paper from the Bartol Research Institute at the University of Delaware.

The IceCube collaboration also acknowledges support from the following agencies. United States: National Science Foundation (NSF) Office of Polar Programs, NSF Physics Division, Wisconsin Alumni Research Foundation, Center for High Throughput Computing (CHTC) at the University of WisconsinMadison, Open Science Grid (OSG), Extreme Science and Engineering Discovery Environment (XSEDE), U.S. Department of Energy National Energy Research Scientific Computing Center, particle astrophysics research computing center at the University of Maryland, Institute for Cyber-Enabled Research at Michigan State University, and the astroparticle physics computational facility at Marquette University. Belgium: Funds for Scientific Research (FRS-FNRS and FWO), FWO Odysseus and Big Science programmes, and Belgian Federal Science Policy Office (Belspo). Germany: Bundesministerium fr Bildung und Forschung (BMBF), Deutsche Forschungsgemeinschaft (DFG), Helmholtz Alliance for Astroparticle Physics (HAP), Initiative and Networking Fund of the Helmholtz Association, Deutsches Elektronen Synchrotron (DESY), and High Performance Computing cluster of the RWTH Aachen. Sweden: Swedish Research Council, Swedish Polar Research Secretariat, Swedish National Infrastructure for Computing (SNIC), and Knut and Alice Wallenberg Foundation. Australia: Australian Research Council. Canada: Natural Sciences and Engineering Research Council of Canada, Calcul Qubec, Compute Ontario, Canada Foundation for Innovation, WestGrid, and Compute Canada. Denmark: Villum Fonden, Danish National Research Foundation (DNRF). New Zealand: Marsden Fund. Japan: Japan Society for Promotion of Science (JSPS) and Institute for Global Prominent Research (IGPR) of Chiba University. Korea: National Research Foundation of Korea (NRF). Switzerland: Swiss National Science Foundation (SNSF).

[1] G. V. Kulikov and G. B. Khristiansen, On the size distribution of extensive atmospheric showers, Zhur. Eksptl'. i Teoret. Fiz. **35**, (1958).

[2] B. Peters, Primary cosmic radiation and extensive air showers, Il Nuovo Cimento (1955-1965) **22**, 800 (1961).

[3] A. M. Hillas, Where do 10^{19} eV cosmic rays come from?, Nuclear Physics B - Proceedings Supplements **136**, 139 (2004).

[4] B. B. *et al.* (ARGO-YBJ), The analog Resistive Plate Chamber detector of the ARGO-YBJ experiment, Astropart. Phys. **67**, 47 (2015), arXiv:1504.01510 [astro-ph.IM].

[5] G. Di Sciasco *et al.* (ARGO-YBJ), Measurement of the Cosmic Ray Energy Spectrum with ARGO-YBJ, in *Pro-*

ceedings, Vulcano Workshop 2014: Frontier Objects in Astrophysics and Particle Physics: Vulcano, Italy, May 18-24, 2014 (2014) arXiv:1408.6739 [astro-ph.HE].

[6] E. de la Fuente *et al.*, The high altitude water čerenkov (hawc) tev gamma ray observatory, in *Cosmic Rays in Star-Forming Environments*, edited by D. F. Torres and O. Reimer (Springer Berlin Heidelberg, Berlin, Heidelberg, 2013) pp. 439–446.

[7] D. Zaborov *et al.* (HAWC), The HAWC observatory as a GRB detector, in *Proceedings, 4th International Fermi Symposium: Monterey, California, USA, October 28-November 2, 2012* (2013) arXiv:1303.1564 [astro-ph.HE].

[8] R. Alfaro *et al.* (HAWC), All-particle cosmic ray energy spectrum measured by the HAWC experiment from 10 to 500 TeV, Phys. Rev. **D96**, 122001 (2017), arXiv:1710.00890 [astro-ph.HE].

[9] T. Antoni *et al.* (KASCADE), The Cosmic ray experiment KASCADE, Nucl. Instrum. Meth. **A513**, 490 (2003).

[10] J. Huang *et al.* (Tibet ASgamma), Measurement of high energy cosmic rays by the new Tibet hybrid experiment, *The Fluorescence detector Array of Single-pixel Telescopes: Contributions to the 35th International Cosmic Ray Conference (ICRC 2017)*, PoS **ICRC2017**, 484 (2018).

[11] N. Budnev *et al.*, The Tunka detector complex: from cosmic-ray to gamma-ray astronomy, *Proceedings, 24th European Cosmic Ray Symposium (ECRS 2014): Kiel, Germany, September 1-5, 2014*, J. Phys. Conf. Ser. **632**, 012034 (2015).

[12] T. Antoni *et al.* (KASCADE), KASCADE measurements of energy spectra for elemental groups of cosmic rays: Results and open problems, Astropart. Phys. **24**, 1 (2005), arXiv:astro-ph/0505413 [astro-ph].

[13] M. A. *et al.* (Tibet ASgamma), Cosmic-ray energy spectrum around the knee obtained by the Tibet experiment and future prospects, Adv. Space Res. **47**, 629 (2011).

[14] M. Amenomori *et al.* (TIBET III), The All-particle spectrum of primary cosmic rays in the wide energy range from 10^{14} eV to 10^{17} eV observed with the Tibet-III air-shower array, Astrophys. J. **678**, 1165 (2008), arXiv:0801.1803 [hep-ex].

[15] T. Abu-Zayyad *et al.* (Telescope Array), The surface detector array of the Telescope Array experiment, Nucl. Instrum. Meth. **A689**, 87 (2013), arXiv:1201.4964 [astro-ph.IM].

[16] A. Aab *et al.* (Pierre Auger), The Pierre Auger Cosmic Ray Observatory, Nucl. Instrum. Meth. **A798**, 172 (2015), arXiv:1502.01323 [astro-ph.IM].

[17] V. Verzi, D. Ivanov, and Y. Tsunesada, Measurement of Energy Spectrum of Ultra-High Energy Cosmic Rays, PTEP **2017**, 12A103 (2017), arXiv:1705.09111 [astro-ph.HE].

[18] P. Abreu *et al.* (Pierre Auger), Measurement of the Cosmic Ray Energy Spectrum Using Hybrid Events of the Pierre Auger Observatory, Eur. Phys. J. Plus **127**, 87 (2012), arXiv:1208.6574 [astro-ph.HE].

[19] M. G. Aartsen *et al.* (IceCube), Measurement of the cosmic ray energy spectrum with IceTop-73, Phys. Rev. **D88**, 042004 (2013), arXiv:1307.3795 [astro-ph.HE].

[20] M. G. Aartsen *et al.* (IceCube), Cosmic Ray Spectrum and Composition from PeV to EeV Using 3 Years of Data From IceTop and IceCube, (2019), arXiv:1906.04317 [astro-ph.HE].

[21] L. . Breiman, Random Forests, Machine Learning **45**, 5 (2001).

[22] M. G. Aartsen *et al.* (IceCube), The IceCube Neutrino Observatory: Instrumentation and Online Systems, JINST **12** (03), P03012, arXiv:1612.05093 [astro-ph.IM].

[23] R. Abbasi *et al.* (IceCube), IceTop: The surface component of IceCube, Nucl. Instrum. Meth. **A700**, 188 (2013), arXiv:1207.6326 [astro-ph.IM].

[24] R. Abbasi *et al.* (IceCube), All-particle cosmic ray energy spectrum measured with 26 IceTop stations, Astropart. Phys. **44**, 40 (2013), arXiv:1202.3039 [astro-ph.HE].

[25] R. Abbasi *et al.* (IceCube), Cosmic ray composition and energy spectrum from 1-30 PeV using the 40-string configuration of IceTop and IceCube, Astroparticle Physics **42**, 15 (2013), arXiv:1207.3455 [astro-ph.HE].

[26] T. K. Gaisser, T. Stanev, T. Waldenmaier, and X. Bai (IceCube), IceTop/IceCube coincidences, in *Proceedings, 30th International Cosmic Ray Conference (ICRC 2007): Merida, Yucatan, Mexico, July 3-11, 2007*, Vol. 5 (2007) pp. 1209–1212.

[27] M. G. Aartsen *et al.* (IceCube), Search for PeV Gamma-Ray Emission from the Southern Hemisphere with 5 Years of Data from the IceCube Observatory, (2019), arXiv:1908.09918 [astro-ph.HE].

[28] R. Abbasi *et al.* (IceCube), Solar Energetic Particle Spectrum on 13 December 2006 Determined by IceTop, Astrophys. J. **689**, L65 (2008), arXiv:0810.2034 [astro-ph].

[29] D. Tosi and H. Pandya (IceCube), IceTop as veto for IceCube: results, in *36th International Cosmic Ray Conference (ICRC 2019) Madison, Wisconsin, USA, July 24-August 1, 2019* (2019) arXiv:1908.07008 [astro-ph.HE].

[30] J. G. Gonzalez for the IceCube Collaboration, Muon Measurements with IceTop, in *European Physical Journal Web of Conferences*, Vol. 208 (2019) p. 03003.

[31] R. Abbasi *et al.* (IceCube), Calibration and characterization of the IceCube photomultiplier tube, Nuclear Instruments and Methods in Physics Research Section A: Accelerators, Spectrometers, Detectors and Associated Equipment **618**, 139152 (2010).

[32] R. Abbasi *et al.* (IceCube), The IceCube Data Acquisition System: Signal Capture, Digitization, and Timestamping, Nucl. Instrum. Meth. **A601**, 294 (2009), arXiv:0810.4930 [physics.ins-det].

[33] E. Ahn, R. Engel, T. K. Gaisser, P. Lipari, and T. Stanev, Cosmic ray interaction event generator SIBYLL 2.1, Phys. Rev. D **80**, 094003 (2009).

[34] S. Ostapchenko, Air shower development: impact of the LHC data, in *Proceedings, 32nd International Cosmic Ray Conference (ICRC 2011): Beijing, China, August 11-18, 2011*, Vol. 2 (2011) p. 71.

[35] D. Heck, J. Knapp, J. N. Capdevielle, G. Schatz, and T. Thouw, CORSIKA: A Monte Carlo code to simulate extensive air showers, (1998).

[36] S. Agostinelli (GEANT4), GEANT4: A Simulation toolkit, Nucl. Instrum. Meth. **A506**, 250 (2003).

[37] G. James, D. Witten, T. Hastie, and R. Tibshirani, *An Introduction to Statistical Learning: With Applications in R* (Springer Publishing Company, Incorporated, 2014) pp. 303–335.

[38] G. Louppe, L. Wehenkel, A. Sutera, and P. Geurts, Understanding variable importances in forests of randomized trees, in *Advances in Neural Information Processing Systems 26*, edited by C. J. C. Burges, L. Bottou, M. Welling, Z. Ghahramani, and K. Q. Weinberger (Curran

Associates, Inc., 2013) pp. 431–439.
[39] X. Meng *et al.*, MLlib: Machine Learning in Apache Spark, J. Mach. Learn. Res. **17**, 1235 (2016).
[40] F. Pedregosa *et al.*, Scikit-learn: Machine Learning in Python, J. Mach. Learn. Res. **12**, 2825 (2011).
[41] G. D'Agostini, A Multidimensional unfolding method based on Bayes' theorem, Nucl. Instrum. Meth. **A362**, 487 (1995).
[42] G. D'Agostini, Improved iterative bayesian unfolding, physics.data-an (2010).
[43] J. Bourbeau and Z. Hampel-Arias, Pyunfold: A python package for iterative unfolding, physics.data-an (2018).
[44] H. Jeffreys, An invariant form for the prior probability in estimation problems, Proceedings of the Royal Society of London A, 10.1098/rspa.1946.0056 (1945).
[45] T. K. Gaisser, Spectrum of cosmic-ray nucleons, kaon production, and the atmospheric muon charge ratio, Astropart. Phys. **35**, 801 (2012), arXiv:1111.6675 [astro-ph.HE].
[46] T. K. Gaisser, T. Stanev, and S. Tilav, Cosmic Ray Energy Spectrum from Measurements of Air Showers, Front. Phys.(Beijing) **8**, 748 (2013), arXiv:1303.3565 [astro-ph.HE].
[47] H. Dembinski *et al.*, Data-driven model of the cosmic-ray flux and mass composition from 10 GeV to 10^{11} GeV, *The Fluorescence detector Array of Single-pixel Telescopes: Contributions to the 35th International Cosmic Ray Conference (ICRC 2017)*, PoS **ICRC2017**, 533 (2018), arXiv:1711.11432 [astro-ph.HE].
[48] T. Antoni *et al.* (KASCADE), KASCADE measurements of energy spectra for elemental groups of cosmic rays: Results and open problems, Astropart. Phys. **24**, 1 (2005), arXiv:astro-ph/0505413 [astro-ph].
[49] V. V. Prosin *et al.*, Tunka-133: Results of 3 year operation, NIM **756**, 94 (2014).
[50] M. Amenomori *et al.* (TIBET III), The All-particle spectrum of primary cosmic rays in the wide energy range from 10^{14} eV to 10^{17} eV observed with the Tibet-III air-shower array, Astrophys. J. **678**, 1165 (2008), arXiv:0801.1803 [hep-ex].
[51] A. D. Panov *et al.*, Energy spectra of abundant nuclei of primary cosmic rays from the data of ATIC-2 experiment: Final results, Bull. Russ. Acad. Sci. Phys **73**, 564 (2009), arXiv:1101.3246 [astro-ph.HE].

Appendix A: Resolutions, Correction Factor, Systematic Uncertainty, and the Final Results

TABLE III. Quality of reconstruction. The first row shows the core resolution in meter. The second row shows the zenith resolution in degree. The third row shows the energy resolution. All these resolutions are one sigma of true minus reconstructed value.

log[E/GeV]	5.4-5.6	5.6-5.8	5.8-6.0	6.0-6.2	6.2-6.4	6.4-6.6	6.6-6.8	6.8-7.0
Core [m]	15.62	13.85	12.03	9.76	8.45	7.76	6.95	6.22
Zenith [deg]	3.95	3.47	2.87	2.51	1.94	1.95	1.62	1.46
Energy	0.26	0.24	0.20	0.16	0.14	0.12	0.10	0.09

TABLE IV. Correction factor on the final flux due to difference in atmospheric pressure between simulation and 2016 data.

$\log_{10}[E/\mathrm{GeV}]$	5.4-5.6	5.6-5.8	5.8-6.0	6.0-6.2	6.2-6.4	6.4-6.6	6.6-6.8	6.8-7.0
[%]	-7.06	-7.41	-7.64	-7.61	-7.50	-7.73	-8.29	-8.16

TABLE V. Total systematic uncertainty after adding individual systematic uncertainty in quadrature.

$\log_{10}[E/\mathrm{GeV}]$	5.4-5.6	5.6-5.8	5.8-6.0	6.0-6.2	6.2-6.4	6.4-6.6	6.6-6.8	6.8-7.0
Low [%]	7.34	7.73	8.56	7.95	5.53	3.40	3.25	3.18
High [%]	6.63	7.49	3.93	4.70	5.44	4.98	6.49	6.89

TABLE VI. Information related to all-particle cosmic ray energy spectrum using two stations events. Sibyll2.1 is the hadronic interaction model assumption. Refer to the text for detail description of each column.

$\log_{10}[E/\mathrm{GeV}]$	N_{events}	Rate [Hz]	Unfolded Rate [Hz]	Flux $[\mathrm{m}^{-2}\mathrm{s}^{-1}\mathrm{sr}^{-1}]$	Stat. Err	Sys Low	Sys High
5.4 - 5.6	3,301,846	1.1566e-1	1.2736e-1	2.1083e-5	1.7635e-8	1.5460e-6	1.3972e-6
5.6 - 5.8	2,034,816	7.1275e-2	8.2527e-2	9.7936e-6	1.2604e-8	7.5661e-7	7.3290e-7
5.8 - 6.0	1,120,920	3.9263e-2	4.6980e-2	4.8085e-6	9.2579e-9	4.1143e-7	1.8871e-7
6.0 - 6.2	527,453	1.8475e-2	2.3303e-2	2.2562e-6	5.5110e-9	1.7938e-7	1.0599e-7
6.2 - 6.4	238,890	8.3678e-3	1.0518e-2	9.9927e-7	3.1977e-9	5.5234e-8	5.4377e-8
6.4 - 6.6	124,673	4.3670e-3	4.6625e-3	4.3873e-7	2.1000e-9	1.4916e-8	2.1847e-8
6.6 - 6.8	52,619	1.8431e-3	1.9715e-3	1.8393e-7	1.3486e-9	5.9861e-9	1.1946e-8
6.8 - 7.0	19,016	6.6661e-4	7.6588e-4	7.1496e-8	7.6165e-10	2.2709e-9	4.9295e-9

TABLE VII. Information related to all-particle cosmic ray energy spectrum using two stations events. QGSJetII-04 is the hadronic interaction model assumption. Refer to the text for detail description of each column.

$\log_{10}[E/\mathrm{GeV}]$	N_{events}	Rate [Hz]	Unfolded Rate [Hz]	Flux $[\mathrm{m}^{-2}\mathrm{s}^{-1}\mathrm{sr}^{-1}]$	Stat. Err	Sys Low	Sys High
5.4 - 5.6	3,476,123	1.2176e-1	1.1476e-1	2.1114e-5	1.3439e-8	3.5836e-6	2.0606e-6
5.6 - 5.8	2,731,596	9.5682e-2	7.7057e-2	9.0641e-6	7.3190e-9	1.1662e-6	8.7336e-7
5.8 - 6.0	1,243,001	4.3539e-2	4.5429e-2	4.4809e-6	5.3524e-9	6.4574e-7	3.9000e-7
6.0 - 6.2	484,928	1.6986e-2	2.3335e-2	2.1778e-6	4.2161e-9	3.4274e-7	1.9567e-7
6.2 - 6.4	269,906	9.4542e-3	1.0467e-2	9.6204e-7	2.3727e-9	1.2298e-7	7.7611e-8
6.4 - 6.6	107,815	3.7765e-3	4.1010e-3	3.7423e-7	1.2508e-9	3.4625e-8	2.9659e-8
6.6 - 6.8	48,760	1.7079e-3	1.6857e-3	1.5268e-7	8.3733e-10	1.2072e-9	1.4139e-8
6.8 - 7.0	18,932	6.6314e-4	6.8663e-4	6.2258e-8	5.6938e-10	4.4720e-9	5.8468e-9

Appendix B: Experimental Data and Simulation Comparison

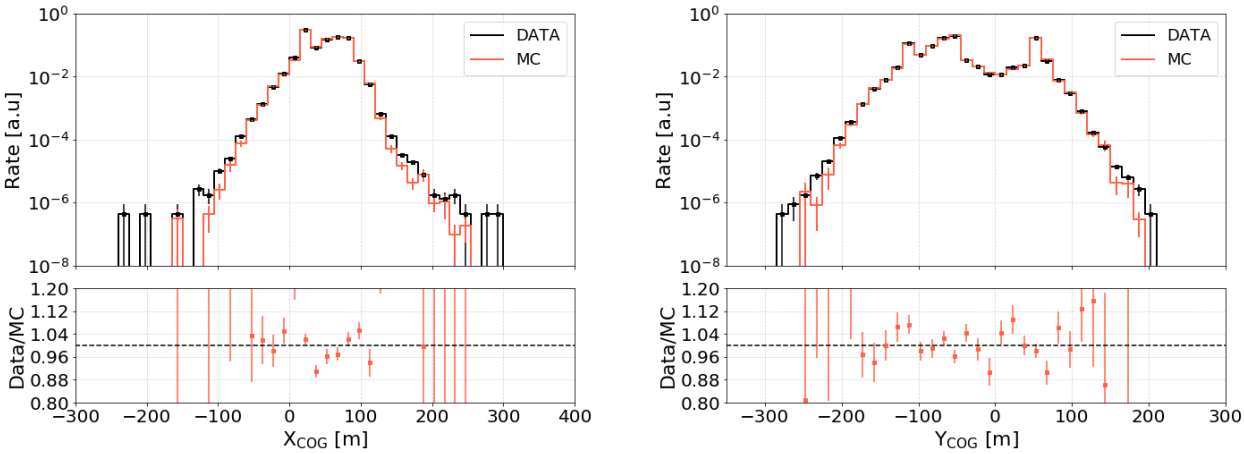

FIG. 13. Histograms of the core positions of showers calculated using Eq. 2 from experimental data and simulation. The left plot is the x-coordinate and the right plot is the y-coordinate of shower's core. Peaks seen on histograms from both plots is due to a larger number of tanks around that x or y coordinate. Refer to Fig 1 for positions of all tanks.

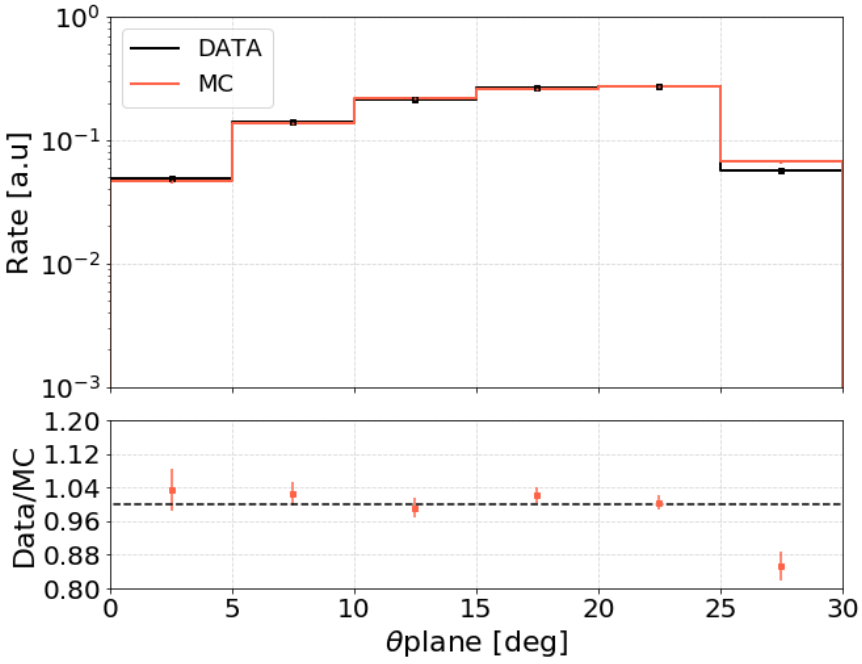

FIG. 14. Histograms of zenith angle calculated assuming plane shower front.

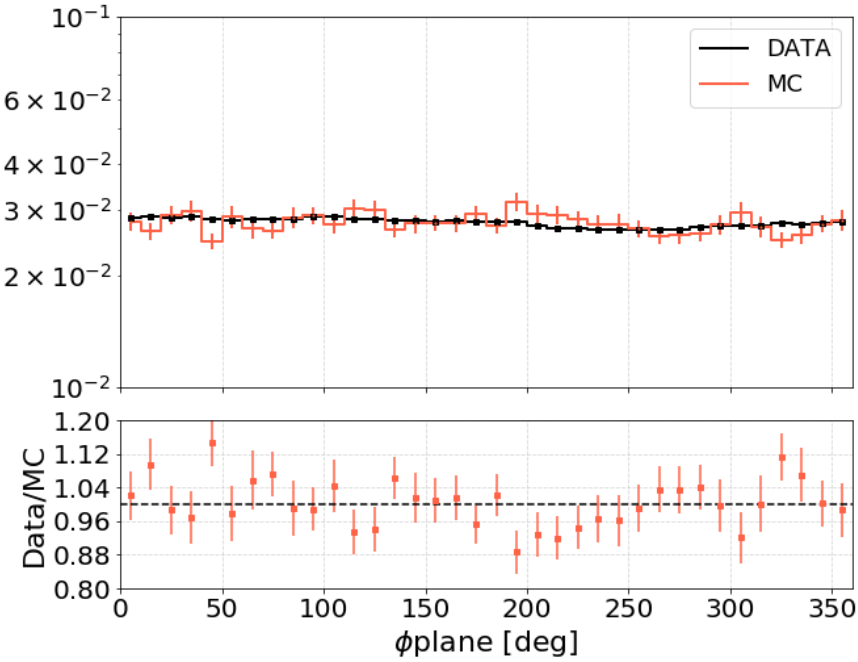

FIG. 15. Histograms of azimuth angle calculated assuming plane shower front.

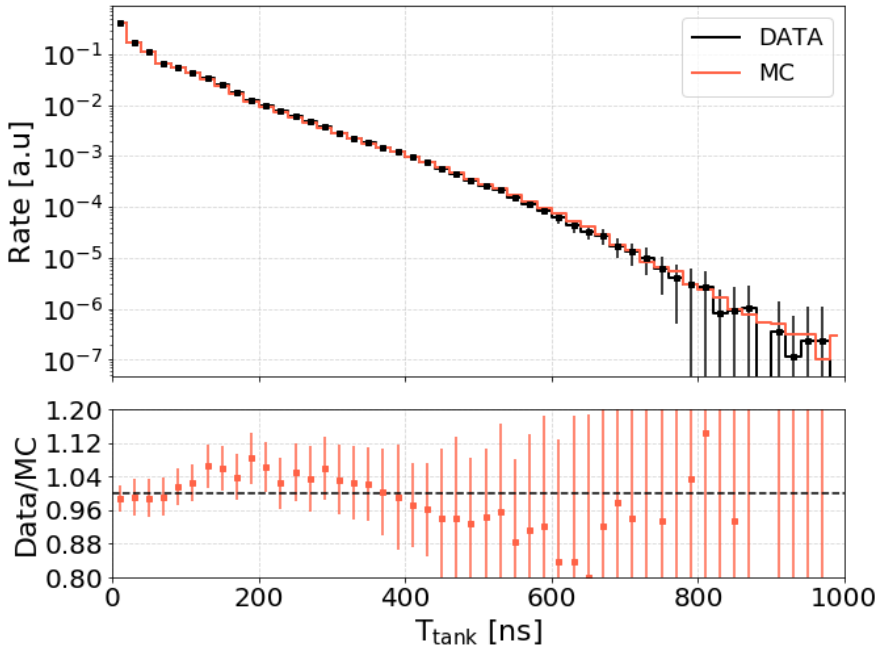

FIG. 16. Histograms of time difference of hits on each tank with respect to the first hit. Time of hits on each tank of an event is listed and sorted in ascending order. The time difference is with respect to the first hit. Time on hit tanks has high feature importance while reconstructing zenith angle.

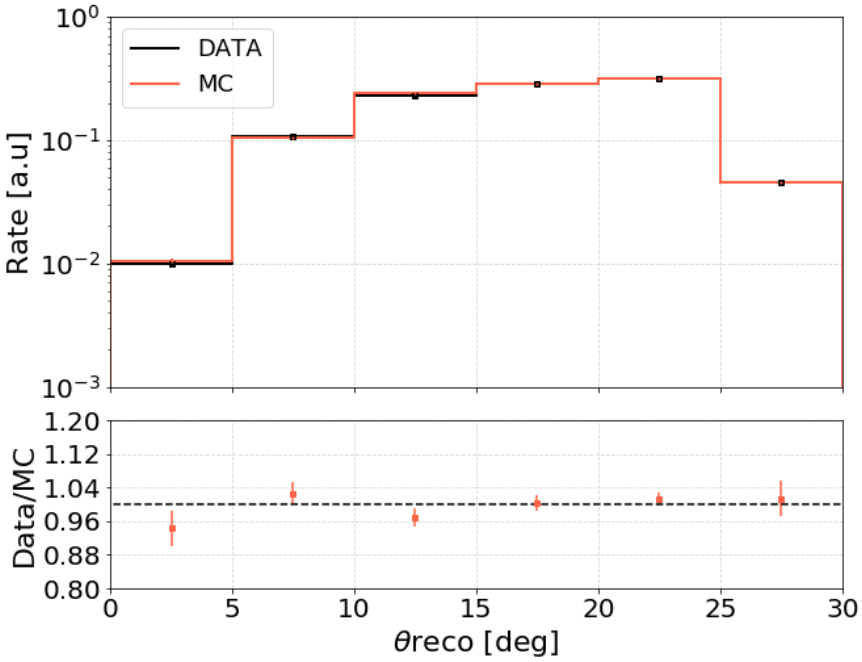

FIG. 17. Histograms of reconstructed zenith angle for experimental data and simulation. Cosine of reconstructed zenith angle is the third important feature while reconstructing energy.

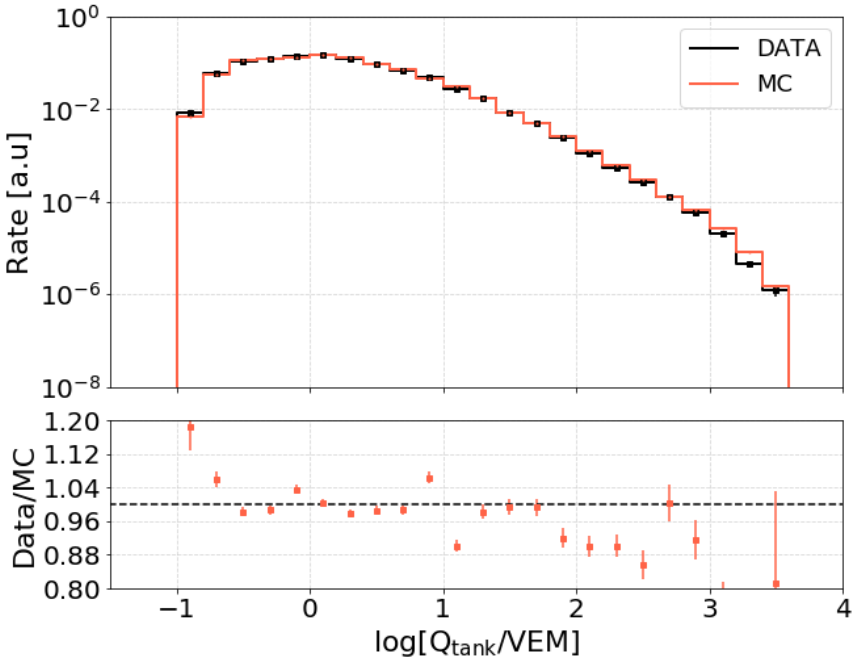

FIG. 18. Histograms of charge deposited on hit tanks. Charge on tanks has a high feature importance while reconstructing shower's energy. Charge less than 0.16 VEM on a tank is considered due to background noise.

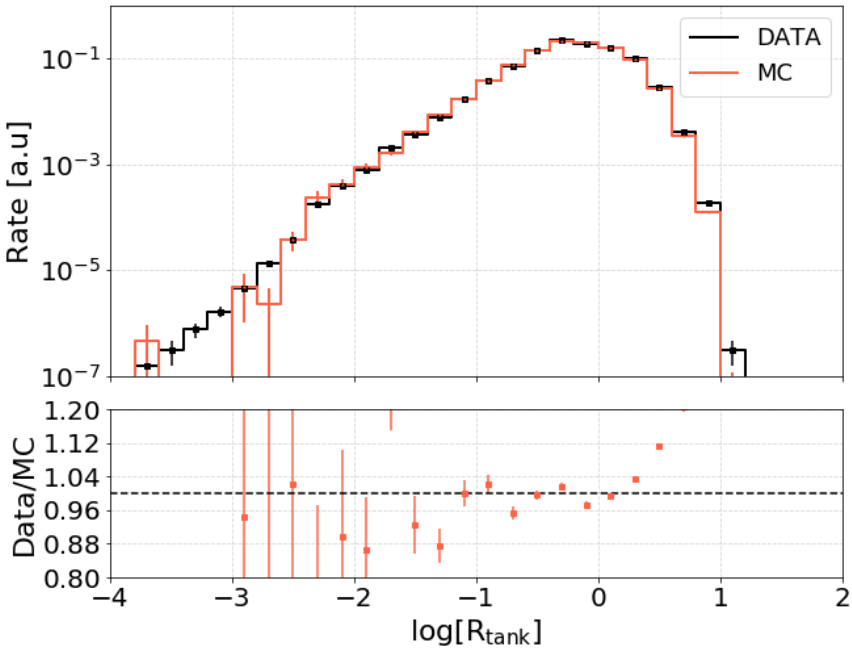

FIG. 19. Histograms of the distance of hit tanks from the reconstructed shower core. The distance is divided by a reference distance of 60 m. The list of distance of hit tanks from the core has high feature importance while reconstructing shower's energy.

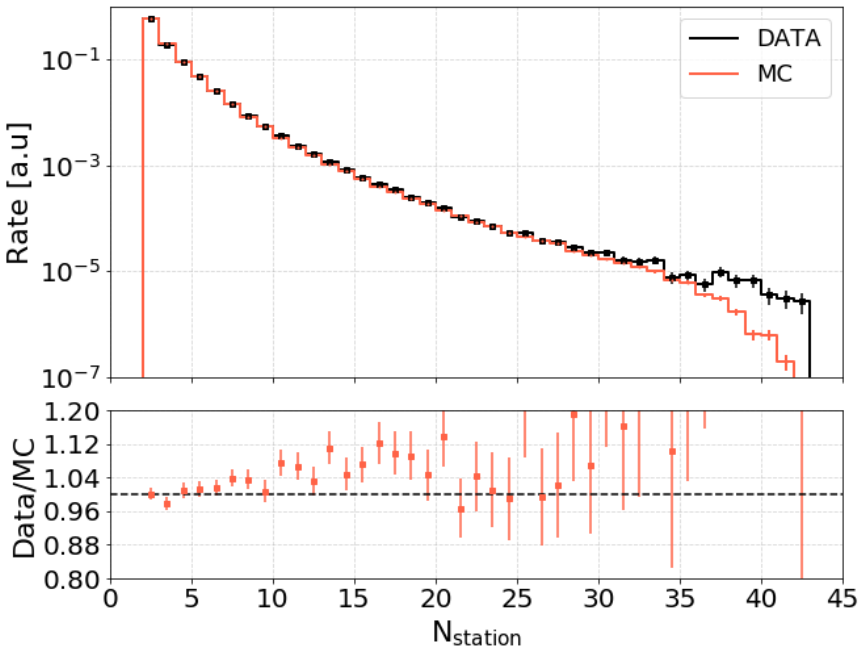

FIG. 20. Histograms of total number of stations hit. It has comparatively small feature importance while predicting energy.

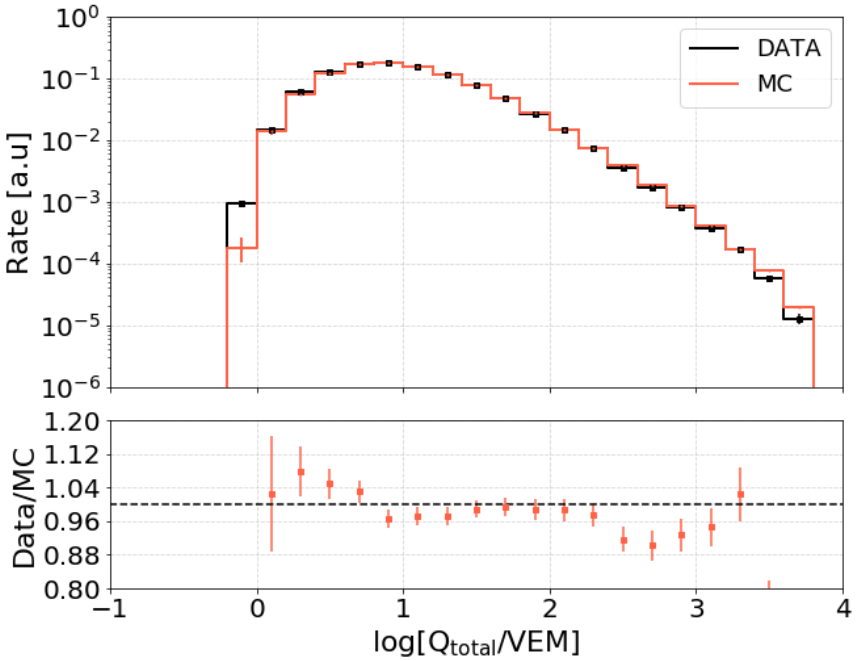

FIG. 21. Histograms of the total amount of charge deposited in all stations. It has comparatively small feature importance while predicting energy.